

Orbital Edelstein effect from density-wave order

Geremia Massarelli,¹ Bryce Wu,¹ and Arun Paramakanti¹

¹*Department of Physics, University of Toronto, Toronto, Ontario M5S 1A7, Canada*

Coupling between charge and spin, and magnetoelectric effects more generally, have been an area of great interest for several years, with the sought-after ability to control magnetic degrees of freedom via charge currents serving as an impetus. The orbital Edelstein effect (OEE) is a kinetic magnetoelectric effect consisting of a bulk orbital magnetization induced by a charge current. It is the orbital analogue of the spin Edelstein effect in spin-orbit coupled materials, in which a charge current drives nonzero electron spin magnetization. The OEE has recently been investigated in the context of Weyl semimetals and Weyl metals. Motivated by these developments, we study a model of electrons without spin-orbit coupling which exhibits line nodes that get gapped out by via symmetry breaking due to an interaction-induced charge density wave order. This model is shown to exhibit a temperature dependent OEE, which appears due to symmetry reduction into a gyrotropic crystal class.

I. INTRODUCTION

The field of magnetoelectric effects has seen a revival in interest in the past decades on several fronts. The discovery and study of multiferroicity in correlated materials has uncovered unconventional mechanisms which can give rise to a large effective magnetoelectric coupling^{1–8}. Similarly, the discovery of three-dimensional (3D) topological insulators has led to an exploration of novel magnetoelectric effects due to emergent axion electrodynamics in such topological phases^{9–18}. A part of the reason for the wide interest in such magnetoelectric effects partly stems from the technological potential of controlling charge degrees of freedom via magnetic fields or, conversely, tuning magnetic degrees of freedom via an applied electric field.

A prominent example of such a magnetoelectric effect is the nonequilibrium phenomenon of current-induced magnetization, which is also termed as *kinetic magnetoelectric effect* (KME)^{19,20}. The intrinsic-spin variant of this effect, wherein a charge current in a spin-orbit-coupled conductor gives rise to bulk spin polarization and, hence, a net magnetization, is referred to as the *Edelstein effect* or the *inverse spin-galvanic effect*^{21,22} and has been under study for several decades²³. A great deal of experimental work has focused on the Edelstein effect in 2D systems, notably in thin-film semiconductors^{24–29} and at metal surfaces³⁰. However, experiments on 3D materials have been scant, although some recent studies have reported its observation in trigonal tellurium^{31,32}.

In recent years, it has come to light that 3D systems can have an intrinsic orbital contribution to the KME, analogous to the spin part and arising as a consequence of the orbital magnetic moment of Bloch bands^{20,33–40}, notably in trigonal selenium and tellurium. Whereas the ordinary Edelstein effect (hereafter referred to as the *spin Edelstein effect*, SEE) relies on crystalline spin-orbit coupling (SOC) to give Bloch states a spin texture and, hence, is limited by the size of the SOC, the *orbital Edelstein effect* (OEE), also referred to as the *inverse gyrotropic magnetic effect*³⁴, is determined solely by the geometry of the crystal^{33,36}.

Chiral crystals are a subset of those that can exhibit the KME. Previous studies have considered trigonal selenium and tellurium and viewed their chiral nature as descending from a charge-density-wave (CDW) instability of a hypothetical parent phase⁴¹, and others have studied optical gyrotropy as a probe for symmetry breaking in the chiral CDW phase of 1T-TiSe₂⁴² and in stripe-ordered cuprates⁴³. It has also been shown that Weyl nodes at the Fermi level can yield a large intrinsic contribution to the KME^{33,36}.

Our work builds on this theme, and explores the KME induced by symmetry breaking in a system with line nodes in the electronic band structure. The resulting phase is a non-chiral but gyrotropic crystal, and we study the concomitant temperature-dependent KME as a probe of the density-wave order. Below, we briefly review the OEE, before introducing our model Hamiltonian and presenting its theoretical study.

II. ORBITAL EDELSTEIN EFFECT

Electrons in crystalline solids form Bloch bands with an intrinsic spin magnetic moment

$$\mathbf{s}_{\mathbf{k}n} = \frac{ge}{2m_e} \langle u_{\mathbf{k}n} | \mathbf{s} | u_{\mathbf{k}n} \rangle, \quad (1)$$

where $\mathbf{s} = \hbar\boldsymbol{\sigma}/2$ is the spin operator for the electrons. The modern theory of magnetization in solids^{44–47} has discovered that such Bloch bands also host an intrinsic orbital magnetic moment given by

$$\mathbf{m}_{\mathbf{k}n} = \frac{e}{2\hbar} \text{Im} \langle \nabla_{\mathbf{k}} u_{\mathbf{k}n} | \times (H_{\mathbf{k}} - \varepsilon_{\mathbf{k}n}) | \nabla_{\mathbf{k}} u_{\mathbf{k}n} \rangle, \quad (2)$$

where $H_{\mathbf{k}}$ is the Bloch Hamiltonian, n is the band index, and $H_{\mathbf{k}} | u_{\mathbf{k}n} \rangle = \varepsilon_{\mathbf{k}n} | u_{\mathbf{k}n} \rangle$. This orbital magnetization has been shown to arise from the self-rotation of wavepackets in the semiclassical theory of electron dynamics^{45,48}. Since $\mathbf{m}_{\mathbf{k}n} \rightarrow -\mathbf{m}_{-\mathbf{k}n}$ under time reversal and $\mathbf{m}_{\mathbf{k}n} \rightarrow \mathbf{m}_{-\mathbf{k}n}$ under spatial inversion, it is clear that at least one of these symmetries must be broken in order for $\mathbf{m}_{\mathbf{k}n}$ to not be identically zero.

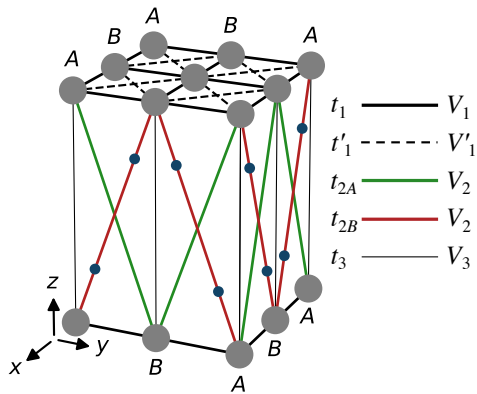


FIG. 1. (Color online) Tetragonal crystal structure showing identical atoms (large gray spheres) on the two sublattices, with a legend for hopping amplitudes and repulsion strengths. Primitive translations \mathbf{a} , \mathbf{b} , and \mathbf{c} are defined in the main text. The volume shown corresponds to two primitive lattice cells. The secondary atoms (small dark-blue spheres) are *not* considered in the model—see text for a discussion.

From the viewpoint of semiclassical dynamics, given an electron distribution function $f_{\mathbf{k}n}$, the intrinsic contribution to the net electronic magnetization is given by^{20,44,48}

$$\mathbf{M} = \frac{1}{\mathcal{V}} \sum_{\mathbf{k}n} f_{\mathbf{k}n} (\mathbf{m}_{\mathbf{k}n} + \mathbf{s}_{\mathbf{k}n}), \quad (3)$$

where \mathcal{V} is the crystal volume. In thermodynamic equilibrium for a time-reversal symmetric system, the Fermi-Dirac distribution, $f_{\mathbf{k}n}^0 = f(\varepsilon_{\mathbf{k}n} - \mu)$ forces zero a net magnetization $\mathbf{M} = 0$ because of cancellation between contributions from opposite crystal momenta³⁶. However, an asymmetric distribution function, such as that arising from an applied electric field, can generally give rise to nonzero net bulk magnetization.

Explicitly, to lowest order in an applied uniform DC electric field, the distribution function is modified as⁴⁹

$$f_{\mathbf{k}n} = f_{\mathbf{k}n}^0 + e\tau(\mathbf{E} \cdot \mathbf{v}_{\mathbf{k}n}) \left. \frac{df}{d\xi} \right|_{\xi=\varepsilon_{\mathbf{k}n}-\mu}, \quad (4)$$

where $\mathbf{v}_{\mathbf{k}n}$ is the electronic group velocity, τ is the impurity-scattering relaxation time in relaxation-time approximation, and $e > 0$ is the elementary charge. Hence, the magnetization arises as a linear response to an applied electric field,

$$M_\kappa = \alpha_{\kappa\lambda} E_\lambda, \quad (5)$$

with the linear response tensor

$$\alpha_{\kappa\lambda} = \alpha_{\kappa\lambda}^{\text{orb}} + \alpha_{\kappa\lambda}^{\text{spin}} \quad (6a)$$

$$= \tau \frac{e}{\hbar} \sum_{\mathbf{k},n} \left. \frac{df}{d\xi} \right|_{\xi=\varepsilon_{\mathbf{k}n}-\mu} (m_{\mathbf{k}n,\kappa} + s_{\mathbf{k}n,\kappa}) v_{\mathbf{k}n,\lambda}, \quad (6b)$$

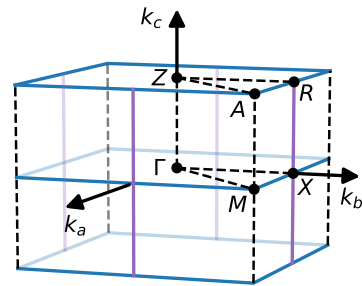


FIG. 2. (Color online) Location of the line nodes (solid lines, shown in color) present in the symmetric phase within the first Brillouin zone for the crystal under study. High-symmetry points are labeled.

where κ and λ are Cartesian indices.

The form of the tensor α is significantly constrained by crystal symmetry^{23,36,50,51}. α is an axial rank-two tensor since it relates a polar vector, \mathbf{E} , to an axial vector, \mathbf{M} . Crystal classes whose point-group symmetries allow for nonzero axial rank-two response tensors are known as *gyrotropic*. The reason for this name is that the tensor governing natural optical activity, or *gyrotropy*, transforms in the same way as α ; thus KME and optical gyrotropy go hand in hand.

We note that the same symmetry constraints govern the appearance of nonzero spin and orbital contributions to α , so both are expected to arise together, and there is no clear route to disentangling them in a 3D system^{32,36}. Indeed, the authors of Ref. 32 conclude by speculating that the current-induced magnetization they observe in trigonal tellurium may be due not only to the well-known SEE, but also to the OEE.

III. MODEL

As an example of the OEE brought about by symmetry breaking, we consider a tight-binding toy model of spinless fermions moving in a tetragonal crystal as shown in Fig. 1, consisting of identical atoms arranged in layered square lattices. We assume a single isotropic orbital, and ignore the electron spin below; there are many cases where this is a useful starting point. In crystals with density-wave order driven by nearest-neighbor repulsion, such as we will consider below, both spin components behave in the same manner. Including spin then only leads to an extra factor-of-two in certain equations below. The other case where spin may be ignored is in spin-polarized systems which might be a useful description of states in a large energy interval around the Fermi energy in strong ferromagnets (i.e., in half-metals).

We define the nearest-neighbor (NN) lattice constant a_0 , and lattice constant along the stacking- \hat{z} axis to be c . In the x - y planes, we include NN hopping t_1 and next-nearest-neighbor (NNN) hopping t'_1 . In the y - z and z - x planes, we include NN hopping t_3 and the peculiar NNN hoppings depicted in

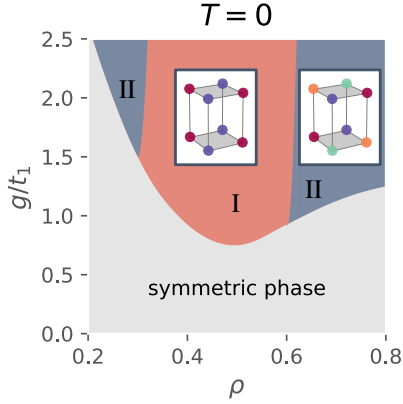


FIG. 3. (Color online) CDW phases arising in the MF study of the Hamiltonian $H = K + V$ at $T = 0$ as a function of the electronic filling ρ and g (which parametrizes the repulsion strength). The nature of phases I and II is described in the text.

Fig. 1, with $t_{2A} \neq t_{2B}$. This last choice differentiates staggered A and B sublattices, and endows the crystal with primitive translations $\mathbf{a} = a_0(\hat{\mathbf{x}} + \hat{\mathbf{y}})$, $\mathbf{b} = a_0(\hat{\mathbf{x}} - \hat{\mathbf{y}})$, and $\mathbf{c} = c\hat{\mathbf{z}}$. The crystal space group is $P4/nbm$, and its associated crystal class is $4/mmm$. Importantly, this crystal has centers of inversion at the middle point of every NN bond.

The inequivalence of the hopping amplitudes t_{2A} and t_{2B} for $P4/nbm$ symmetry may be rationalized as depicted in Fig. 1: if a secondary set of atoms is present only along the red bonds—which would be consistent with the space-group symmetry of the model—and their energy levels are far from the Fermi energy, their dynamics could be integrated out, with the end result of renormalizing the hopping amplitude between the primary atoms (shown in gray), effectively leading to $t_{2A} \neq t_{2B}$. The same reasoning holds if there are additional secondary atoms on the green bonds *provided they are of a species different from those on the red bonds*.

We use the following values for the hopping parameters: $t'_1 = 0.7 t_1$, $t_{2A} = 0.1 t_1$, $t_{2B} = 0.4 t_1$, and $t_3 = 0.5 t_1$.

As is true for any crystal class with inversion symmetry, $4/mmm$ is non-gyrotropic^{50,51}. However, if the symmetry of the crystal were to be reduced, for instance by the onset of CDW order, the inversion symmetry could be broken and, indeed, the ordered structure could fall into a gyrotropic class. Below, we first study the band structure of this model in the absence of interactions, before turning to the impact of nearest-neighbor repulsion.

A. Non-interacting band structure

The non-interacting Hamiltonian is $K = \sum_{i,j} -t_{ij}^{\alpha\beta} c_i^{\alpha\dagger} c_j^\beta$, where $c_i^{\alpha\dagger}$ creates an electron on sublattice α of unit cell i

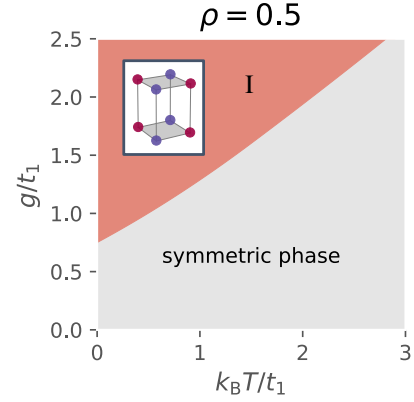


FIG. 4. (Color online) CDW phases arising in the MF study of the Hamiltonian $H = K + V$ at half filling ($\rho = 0.5$) as a function of temperature and g (which parametrizes the repulsion strength). The nature of phase I is described in the text.

(that is, on the atom at position \mathbf{r}_i^α). In momentum space

$$K = \sum_{\mathbf{k}} \psi_{\mathbf{k}}^\dagger \left(d_{\mathbf{k}}^0 + \vec{d}_{\mathbf{k}} \cdot \vec{\tau} \right) \psi_{\mathbf{k}}, \quad (7)$$

$c_{\mathbf{k}}^\alpha = N^{-1/2} \sum_i e^{-i\mathbf{k} \cdot \mathbf{r}_i^\alpha} c_i^\alpha$, N is the number of unit cells, $\vec{\tau}$ is the vector of Pauli matrices (acting in sublattice space), and $\psi_{\mathbf{k}}^\dagger = \left(c_{\mathbf{k}}^{A\dagger} \ c_{\mathbf{k}}^{B\dagger} \right)$. Because of time-reversal symmetry, the hopping amplitudes $t_{ij}^{\alpha\beta}$ are necessarily real valued. We will measure momenta in units of inverse lattice spacing, and henceforth set $a = c = 1$. With this, we arrive at

$$d_{\mathbf{k}}^0 = -2t_3 \cos(k_c) - 2t'_1 \left(\cos(k_a) + \cos(k_b) \right) \quad (8a)$$

$$d_{\mathbf{k}}^1 = -4 \cos\left(\frac{k_a}{2}\right) \cos\left(\frac{k_b}{2}\right) \left(t_1 + (t_{2A} + t_{2B}) \cos(k_c) \right) \quad (8b)$$

$$d_{\mathbf{k}}^2 = 4(t_{2A} - t_{2B}) \cos\left(\frac{k_a}{2}\right) \cos\left(\frac{k_b}{2}\right) \cos(k_c) \quad (8c)$$

$$d_{\mathbf{k}}^3 = 0. \quad (8d)$$

The inversion symmetry I mentioned above combined with the Hamiltonian's time-reversal symmetry Θ constrain $d_{\mathbf{k}}^3 \equiv 0$ identically; for this reason, band touchings for this crystal will generically arise as line nodes, as seen in the non-interacting band structure (top panel of Fig. 6) Figure 2 shows the location of the line nodes in the Brillouin zone.

Spontaneous symmetry breaking (SSB), however, could change the crystal class to a less symmetric one. A simple scenario is a CDW phase in which the densities on the A and B atoms are unequal, in which case the space group becomes $P42m$, whose crystal class— $42m$ —is gyrotropic.

B. Repulsive interactions

Next, we include repulsive interactions between NNs and next-nearest neighbors (NNNs); that is,

$$V = \frac{1}{2} \sum_{(i,\alpha) \neq (j,\beta)} V_{ij}^{\alpha\beta} n_i^\alpha n_j^\beta, \quad (9)$$

where $n_i^\alpha = c_i^{\alpha\dagger} c_i^\alpha$ is the number operator for the atom (i, α) and we take $V_{ij}^{\alpha\beta} = V_{ji}^{\beta\alpha}$. We take nonzero repulsions $V_{ij}^{\alpha\beta}$ on the same bonds as the hopping amplitudes and use a similar naming scheme, as shown in Fig. 1. Note that, unlike for the hopping amplitudes $t_{2A} \neq t_{2B}$, we take the repulsion strengths to be V_2 on both the red and green bonds — we make this choice since it serves as a representative slice through the full parameter space and serves to illustrate some of the key ideas. Hence, the full Hamiltonian is given by $H = K + V$.

In the absence of spin order, a Hubbard term $U \sum_i n_{i\uparrow} n_{i\downarrow}$ would modify the MF Hamiltonian by a mere uniform offset in the chemical potential μ . Hence, as we will restrict ourselves to ansätze without spin order, we do not include the Hubbard interaction.

We performed a MF calculation of the CDW order in the above system, allowing for a finite set of commensurate wavevectors. We identified the ordering wavevectors favoured by the interaction by considering a simple model of classical charges resting at each atomic site of the crystal of Fig. 1—see Appendix A. Based on this, we included in our ansatz the four ordering wavevectors

$$\begin{aligned} \mathbf{Q}_0 &= 0 & \mathbf{Q}_1 &= \pi \hat{\mathbf{a}} + \pi \hat{\mathbf{b}} \\ \mathbf{Q}_2 &= \pi \hat{\mathbf{c}} & \mathbf{Q}_3 &= \pi \hat{\mathbf{a}} + \pi \hat{\mathbf{b}} + \pi \hat{\mathbf{c}}. \end{aligned}$$

The order parameters for the mean-field theory are the Fourier amplitudes $\rho_{\mathbf{Q}}^\alpha$ for the \mathbf{Q} listed above, where $\alpha \in \{A, B\}$. However, we find it convenient to express the amplitudes on the A and B sublattices in terms of a symmetric and an antisymmetric part, respectively defined as

$$\rho_{\mathbf{Q}}^s := \frac{\rho_{\mathbf{Q}}^A + \rho_{\mathbf{Q}}^B}{2}, \quad (10a)$$

$$\rho_{\mathbf{Q}}^a := \frac{\rho_{\mathbf{Q}}^A - \rho_{\mathbf{Q}}^B}{2}. \quad (10b)$$

Since $\rho_{\mathbf{Q}_0}^s = \rho$, the electron filling, we are left with 7 independent MFs.

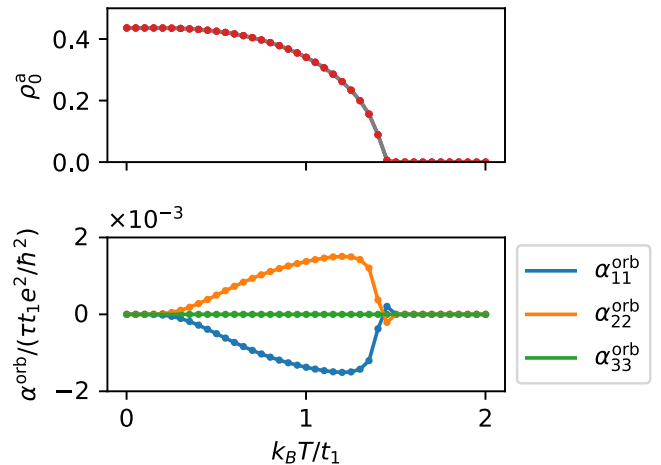


FIG. 5. (Color online) Evolution of the magnetoelectric response through a phase transition with $g = 1.5t_1$ and $\rho = 0.5$. TOP PANEL Order parameter $(\rho_{\mathbf{Q}_0}^a)$ as a function of temperature. BOTTOM PANEL Components of the OEE response tensor α^{orb} as a function of temperature. Components that are not shown are identically zero.

IV. RESULTS

A. Mean-field theory of charge-density-wave order

We focus on a cut of parameter space parametrized by g such that

$$V_1 = g, \quad V_1' = \frac{g}{2}, \quad V_2 = \frac{g}{2}, \quad V_3 = \frac{g}{2}. \quad (11)$$

According to the model of electrostatic charges, at these relative repulsion values (marked by a white star in Fig. 10), the interaction most favours an ordering with $\rho_{\mathbf{Q}_0}^a \neq 0$; however, the region of parameter space with $\rho_{\mathbf{Q}_3}^\alpha \neq 0$ most favoured is nearby (see Appendix A).

The MF calculation, for which the zero-temperature phase diagram is shown in Fig. 3, does indeed identify a swath of pure $\rho_{\mathbf{Q}_0}^a \neq 0$ order for g sufficiently large and for approximately $0.3 < \rho < 0.6$ —call this order *phase I*. In addition to this phase, we discover mixed phases at high and low filling in which both $\rho_{\mathbf{Q}_0}^a \neq 0$ and $\rho_{\mathbf{Q}_3}^\alpha \neq 0$, where α is either A or B —call the order in these regions *phase II*.

For $g/t_1 \gg 1$, we observe that the phase diagram is approximately symmetric under $\rho \rightarrow 0.5 - \rho$; this is expected given the particle-hole symmetry of V , which becomes an approximate symmetry of H when K is nonzero but small compared with V .

The phase diagram at $\rho = 0.5$ as a function of T and g is shown in Fig. 4 and reveals that raising the system temperature progressively suppresses phase-I order.

B. Magnetoelectric response in phase I

We studied the temperature-dependent SSB-induced OEE in broken-symmetry phase I, whose sole order parameter is $\rho_{\mathbf{Q}_0}^a$. Figure 5 shows the evolution of $\rho_{\mathbf{Q}_0}^a$ and the components of the response tensor α^{orb} at half filling ($\rho = 0.5$) and fixed interaction strength ($g = 1.5 t_1$). The phase transition, which is seen to be continuous, takes place at $k_B T_c \approx 1.4 t_1$.

As alluded to previously, the point-group symmetry in phase I is the $\bar{4}2m$, and a symmetry analysis reveals that symmetry constrains the response tensor α to the form⁵⁰

$$\alpha = \begin{pmatrix} \alpha_{aa} & & \\ & -\alpha_{aa} & \\ & & 0 \end{pmatrix}. \quad (12)$$

As seen in the lower panel of Fig. 5, the calculated α^{orb} is indeed of this form. The nonmonotonicity of α^{orb} is understood via the MF band structure, seen in Fig. 6. The top panel shows the high-temperature ($k_B T = 2.00 t_1$) band structure. Although the system is in a metallic phase with many states within $k_B T$ (gray shading) from the chemical potential μ (dotted line), in the high-symmetry phase, $\mathbf{m}_{\mathbf{k}n} = 0$ identically, so $\alpha^{\text{orb}} = 0$. The middle panel shows the band structure at an intermediate temperature $k_B T = 1.20 t_1$ (near the peak in the α^{orb}); the phase-I charge order has broken inversion symmetry and split the bands throughout the Brillouin zone, and the reduced symmetry of phase allows gyrotropic response, so $\alpha^{\text{orb}} \neq 0$. As the temperature is further lowered, the size of the band splitting increases and a full gap develops, with μ within this gap (lower panel of Fig. 5). Hence, it is clear that in the low-temperature limit, as the sum in Eq. 6 approaches a Fermi-surface integral, α^{orb} should again vanish.

C. Role of line nodes

In this subsection, we inspect the contribution of the gapped-out line nodes to the magnetoelectric response tensor α^{orb} in phase I. As depicted in Fig. 2, in the high-symmetry phase, three independent line nodes exist in the first Brillouin zone: 1. the X - R segment, 2. the X - M segment, and 3. the R - A segment—all other line nodes are related by symmetry.

In phase I, the charge order breaks the inversion symmetry Π ; accordingly, in the MF Hamiltonian for phase I, $d_{\mathbf{k}}^3$ is no longer constrained to be zero, so the band touchings disappear. Rather, $d_{\mathbf{k}}^3$ is set by the phase-I order parameter $\rho_{\mathbf{Q}_0}^a$. As a shorthand, define

$$v := \tilde{\rho}_{\mathbf{Q}_0}^a, \quad (13)$$

where $\tilde{\rho}_{\mathbf{Q}_0}^a$, defined in Appendix B, is proportional to the phase-I order parameter $\rho_{\mathbf{Q}_0}^a$.

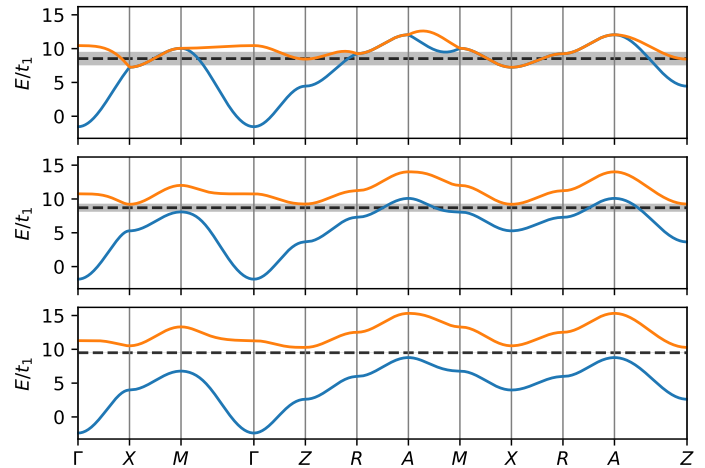


FIG. 6. (Color online) Mean-field band structure at half filling (with parameters as specified in the main text) at three different temperatures: $k_B T/t_1 = 2.00$ (top), 1.20 (middle), and 0.05 (bottom). The black dotted lines show the location of the chemical potential μ at each temperature, and the shaded areas centered at μ show the width $k_B T$.

We expand about the (gapped) line nodes, denoting small deviations in momentum by $\tilde{\mathbf{k}}$. In the neighborhood of the (gapped) nodes, we have

$$1. \quad k_a = \pi + \tilde{k}_a, \quad k_b = \tilde{k}_b, \quad -\pi < k_c \leq \pi$$

$$d_{\mathbf{k}}^0 = -2t_3 \cos(k_c) \quad (14a)$$

$$d_{\mathbf{k}}^1 = 2(t_1 + (t_{2A} + t_{2B}) \cos(k_c)) \tilde{k}_a \quad (14b)$$

$$d_{\mathbf{k}}^2 = 2(t_{2A} - t_{2B}) \sin(k_c) \tilde{k}_b \quad (14c)$$

$$d_{\mathbf{k}}^3 = v \quad (14d)$$

$$2. \quad -\pi < k_a < \pi, \quad k_b = \pi + \tilde{k}_b, \quad k_c = \tilde{k}_c$$

$$d_{\mathbf{k}}^0 = -2t_3 + 2t_1'(1 - \cos(k_a)) \quad (15a)$$

$$d_{\mathbf{k}}^1 = 2(t_1 + t_{2A} + t_{2B}) \cos\left(\frac{k_a}{2}\right) \tilde{k}_b \quad (15b)$$

$$d_{\mathbf{k}}^2 = 4(t_{2A} - t_{2B}) \sin\left(\frac{k_a}{2}\right) \tilde{k}_c \quad (15c)$$

$$d_{\mathbf{k}}^3 = v \quad (15d)$$

$$3. \quad -\pi < k_a < \pi, \quad k_b = \pi + \tilde{k}_b, \quad k_c = \pi + \tilde{k}_c$$

$$d_{\mathbf{k}}^0 = 2t_3 + 2t_1'(1 - \cos(k_a)) \quad (16a)$$

$$d_{\mathbf{k}}^1 = 2(t_1 - t_{2A} - t_{2B}) \cos\left(\frac{k_a}{2}\right) \tilde{k}_b \quad (16b)$$

$$d_{\mathbf{k}}^2 = -4(t_{2A} - t_{2B}) \sin\left(\frac{k_a}{2}\right) \tilde{k}_c \quad (16c)$$

$$d_{\mathbf{k}}^3 = v. \quad (16d)$$

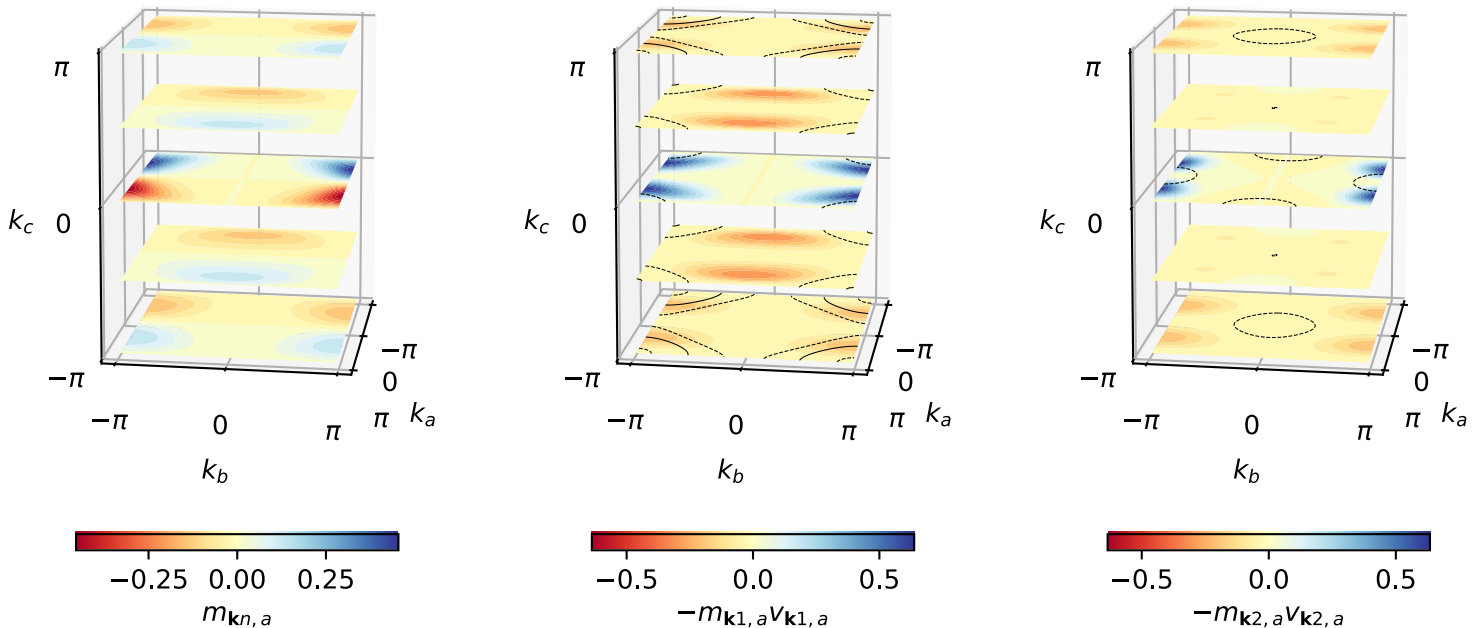


FIG. 7. (Color online) Magnetic moment $m_{\mathbf{k}n,a}$ and product $-m_{\mathbf{k}n,a}v_{\mathbf{k}n,a}$ for bands $n = 1$ and 2 at $k_B T = 1.20 t_1$. As expected, $m_{\mathbf{k}n,a}$ is odd under $k_a \rightarrow -k_a$. The solid lines in middle and right panels depict $\varepsilon_{\mathbf{k}n} = \mu$ surfaces, while the dashed lines show $\varepsilon_{\mathbf{k}n} = \mu \pm k_B T$ surfaces. Other components are either related by symmetry or vanish.

We can compute the orbital magnetic moment about such a (gapped) line node: for a two-band model with Bloch Hamiltonian $H_{\mathbf{k}} = d_{\mathbf{k}}^0 \tau^0 + \vec{d}_{\mathbf{k}} \cdot \vec{\tau}$, $\mathbf{m}_{\mathbf{k}n}$ can be written in the closed form^{34,36}

$$m_{\mathbf{k}n,\kappa} = -\frac{e}{2\hbar} \varepsilon_{\kappa\lambda\zeta} \frac{\vec{d}_{\mathbf{k}}}{|\vec{d}_{\mathbf{k}}|^2} \cdot \left(\frac{\partial \vec{d}_{\mathbf{k}}}{\partial k_\lambda} \times \frac{\partial \vec{d}_{\mathbf{k}}}{\partial k_\zeta} \right), \quad (17)$$

where κ , λ , and ζ are Cartesian indices.

In the neighborhood of a (gapped) line node in the $\hat{\mathbf{a}}$ direction,

$$d_{\mathbf{k}}^0 = f(k_a), \quad \vec{d}_{\mathbf{k}} = (g_1(k_a)\tilde{k}_b, g_2(k_a)\tilde{k}_c, h(k_a)), \quad (18)$$

where f , g_1 , g_2 , and h are functions of k_a , and hence, the components of $\mathbf{m}_{\mathbf{k}n}$ are given by

$$m_{\mathbf{k}n,a} = \frac{e}{2\hbar} \frac{1}{|\vec{d}_{\mathbf{k}}|^2} g_1 g_2 h \quad (19a)$$

$$m_{\mathbf{k}n,b} = \frac{e}{2\hbar} \frac{\tilde{k}_b}{|\vec{d}_{\mathbf{k}}|^2} g_2 (g_1 h' - g_1' h) \quad (19b)$$

$$m_{\mathbf{k}n,c} = \frac{e}{2\hbar} \frac{\tilde{k}_c}{|\vec{d}_{\mathbf{k}}|^2} g_1 (g_2 h' - g_2' h), \quad (19c)$$

where primes denote differentiation of the single-variable functions. To describe a line node in another direction, the indices in Eqs. 18 and 19 must be interchanged appropriately.

Figure 7 shows that the main contributions to α^{orb} originate from the line nodes. The figure, for which we take $k_B T = 1.20 t_1$ as in the middle panel of Fig. 6, shows the orbital magnetic moment $m_{\mathbf{k}n,a}$ (left panel) as well as the product $-m_{\mathbf{k}n,a}v_{\mathbf{k}n,a}$ for the bottom ($n = 1$, middle panel) and top ($n = 2$, top panel) bands, which enter into the calculation of α_{aa}^{orb} . [The component α_{bb}^{orb} is related by symmetry (Eq. 12), while all other components vanish.] These quantities are shown along slices $k_c = -\pi, -\pi/2, 0, \pi/2, \pi$.

The form of $m_{\mathbf{k}n,a}$ in momentum space reflects all the symmetries of the point group $\bar{4}2m$ of phase I. The large values of $m_{\mathbf{k}n,a}$ are attributable to the presence of line nodes and are as expected from Eqs. 19: for the slices $k_c = \pm\pi/2$, we see the signature of the line node transverse to $\hat{\mathbf{a}}$, for which $m_{\mathbf{k}n,a} \rightarrow 0$ in proximity to the node, and for the slices $k_c = 0$ and $k_c = \pm\pi$, we also recognize contributions from the line nodes longitudinal to $\hat{\mathbf{a}}$, which are largest at the locus of the line nodes. The product $-m_{\mathbf{k}n,a}v_{\mathbf{k}n,a}$ still retains the general form of $m_{\mathbf{k}n,a}$, though with a modified symmetry that allows a nonzero integral over the Fermi surface.

The difference in the magnitude of the longitudinal contributions at $k_c = 0$ and $k_c = \pm\pi$ can be retraced to the different $g_1(k_a)$ for the line nodes in those planes: while $g_1(k_a) = 2(t_1 + t_{2A} + t_{2B}) \cos(k_a/2)$ for the former, $g_1(k_a) = 2(t_1 - t_{2A} - t_{2B}) \cos(k_a/2)$ for the latter, and $|t_1 + t_{2A} + t_{2B}| > |t_1 - t_{2A} - t_{2B}|$ with our parameter values.

As shown by Eq. 6, up to constant factors, the integrand for

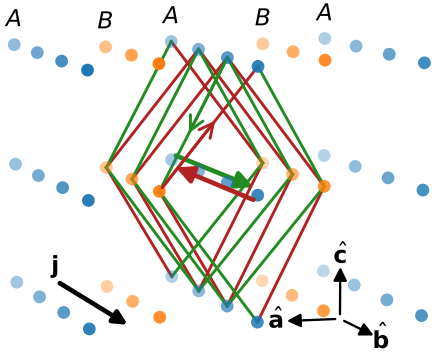


FIG. 8. (Color online) For a current \mathbf{j} oriented in the $\hat{\mathbf{b}}$ direction, solenoid-like paths due to the t_{2A} hoppings (green) and the t_{2B} hoppings (red) have opposite helicity. If $t_{2A} = t_{2B}$, the magnetizations from the two solenoids cancel. Crystal is not drawn to scale.

α_{aa}^{orb} is $-m_{\mathbf{k}n,a}v_{\mathbf{k}n,a}$ multiplied by $-df/d\xi|_{\xi=\varepsilon_{\mathbf{k}n}-\mu}$, a weighting factor concentrated within $k_B T$ around the chemical potential μ . Hence, the equal-energy surfaces at $\varepsilon_{\mathbf{k}n} = \mu$ (solid black lines) and $\varepsilon_{\mathbf{k}n} = \mu \pm k_B T$ (dashed black lines) reveal the main contributions to the integral. At this temperature, for our choice of parameters, the largest contributions to α^{orb} are from the (gapped) line nodes at $k_c = \pm\pi$.

V. DISCUSSION AND CONCLUSION

It is sometimes overlooked that gyrotropy can arise without chiral or time-reversal symmetry breaking^{23,43}. Since the point group $\bar{4}2m$ of the phase I order contains mirror symmetries (in our coordinates, one perpendicular to $\hat{\mathbf{x}}$ and another perpendicular to $\hat{\mathbf{y}}$), the structure of this broken-symmetry phase is an example of a non-chiral gyrotropic structure. This is unlike many of the examples of the OEE studied so far^{33,36}, such as trigonal selenium and tellurium^{20,35}. Furthermore, it constitutes a concrete example of longitudinal magnetization induced by a current in a mirror-symmetric structure, while it has been implied that this is not allowed by symmetry³³. While longitudinal magnetization is forbidden by mirrors perpendicular or parallel to the current, it is not forbidden by mirrors at 45° angles from the current.

Similarly to a previously studied model³⁶, a picture of current flowing through solenoids provides a qualitative understanding of the OEE in phase I. Furthermore, this picture makes physically clearer why the OEE response vanishes (i) when $t_{2A} = t_{2B}$ — hence clarifying physically the necessity of assuming $t_{2A} \neq t_{2B}$ from the start — and (ii) in the absence of charge order, that is, when the atoms are indistinguishable. We imagine a current driven in the $\hat{\mathbf{b}}$ direction: the simplest solenoid-like paths that result in net displacement purely in the $\hat{\mathbf{b}}$ direction are shown in Fig. 8 and 9.

(i) Each row of atoms, whether on sublattice A or B , is

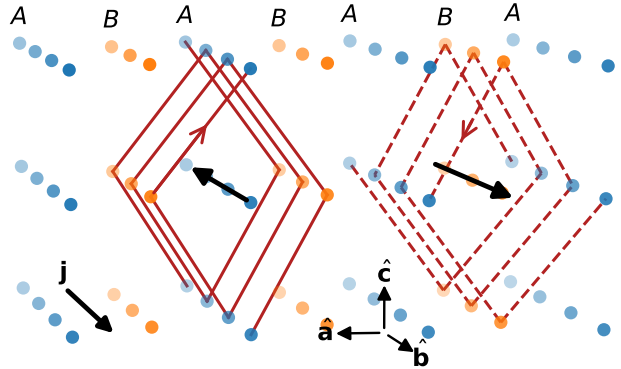


FIG. 9. (Color online) For a current \mathbf{j} oriented in the $\hat{\mathbf{b}}$ direction, solenoid-like paths with their axis along A atoms (solid lines) have opposite helicity to those with their axis along B atoms (dashed lines). If the atoms are indistinguishable, the magnetizations from the two solenoids cancel on average. Crystal is not drawn to scale.

surrounded by a solenoid traced out of t_{2A} (green) hoppings and another traced out of t_{2B} (red) hoppings (Fig. 8). These two solenoids are of opposite helicities, and if $t_{2A} = t_{2B}$, their induced magnetic fields cancel identically, precluding any current-induced magnetization whether in the symmetric phase or in a charge-ordered phase. Indeed, if $t_{2A} = t_{2B}$, there exist additional mirror planes (perpendicular to $\hat{\mathbf{a}}$ and to $\hat{\mathbf{b}}$) that interchange the two solenoids.

(ii) If $t_{2A} \neq t_{2B}$, let us presume without loss of generality that t_{2B} (in red) is dominant and ignore the t_{2A} solenoids. Figure 9 shows that a solenoid whose central axis is a row of A sites is of opposite helicity as one whose central axis is a row of B sites. If the atoms on the two sublattices are indistinguishable, the magnetic fields induced by these two solenoids are equal and opposite and cancel when averaged over several lattice spacings. If the A and B atoms are distinguishable, however, the two sets of solenoids are distinct and can give rise to net magnetization. Indeed, while in the symmetric phase, there exist glide planes perpendicular to $\hat{\mathbf{a}}$ and along $\hat{\mathbf{b}}$ that interchange the dotted-line and solid-line solenoids.

It is surprising *a priori* that such a solenoid picture can exist in a nonchiral crystal (previous examples have focused on chiral structures^{20,33,36}); however, the two mirror symmetries of point group $\bar{4}2m$ —one perpendicular to $\hat{\mathbf{x}}$ and the other perpendicular to $\hat{\mathbf{y}}$ —do not bring the solenoids into themselves, but rather exchange the a -axis solenoids with the b -axis solenoids. The mirrors instead explain why the OEE coefficients along the a and b axis are opposite in sign, since the current is a polar vector and the magnetization is an axial vector.

In summary, we have discussed a simple model of a crystal with line nodes, and shown how charge order can lead to a nonzero OEE. Such an OEE could be probed by nuclear

magnetic resonance experiments. We have also discussed how the magnetoelectric response has a large contribution arising from the vicinity of line nodes. Our work suggests that lightly doped line-node semimetals in materials with weak spin-orbit coupling might be a promising place to search for large OEE.

Note While completing this manuscript, we came across a recent theory preprint⁵² which discusses the OEE induced by quadrupolar symmetry breaking in certain diamond lattice materials.

ACKNOWLEDGEMENTS

We thank D. A. Pesin for fruitful discussions. This research was funded by the Natural Sciences and Engineering Research Council of Canada and the Canadian Institute for Advanced Research. G. M. is supported by the *Fonds de recherche du Québec - Nature et technologies*. This research was enabled in part by support provided by Compute Ontario, Westgrid and Compute Canada. Computations were performed on the Niagara supercomputer at the SciNet HPC Consortium. SciNet is funded by: the Canada Foundation for Innovation; the Government of Ontario; Ontario Research Fund - Research Excellence; and the University of Toronto.

Appendix A: Classical phase diagram

The ordering wavevectors favoured by the interaction of Eq. 9 were identified by determining the energy of CDW modes according to V in a classical picture of electrostatic charges. In Fig. 10, we show which mode has the lowest energy (according to V) as a function of the (relative) sizes of the repulsion strengths V_1 , V_1' , V_2 , and V_3 . Note that, unlike in the main text, the modes are given in x - y - z coordinates as (Q_x, Q_y, Q_z) (where we have set $a_0 = c = 1$), since it is not necessary to work with a multi-atom basis when considering only the repulsion term V . Furthermore, note that the yellow phase $(\pi, 0, \pi)$ implicitly stands for itself as well as its symmetry-related counterpart $(0, \pi, \pi)$; the two are degenerate as expected by symmetry.

The ansatz for the mean-field theory described in the main text was chosen to potentially allow all the ground states that occur in this simplified model.

Appendix B: Details of the mean-field calculation

Here, we provide additional information regarding the self-consistent MF calculation of the CDW order. The interaction of Eq. 9 was decomposed in the density channel, giving rise

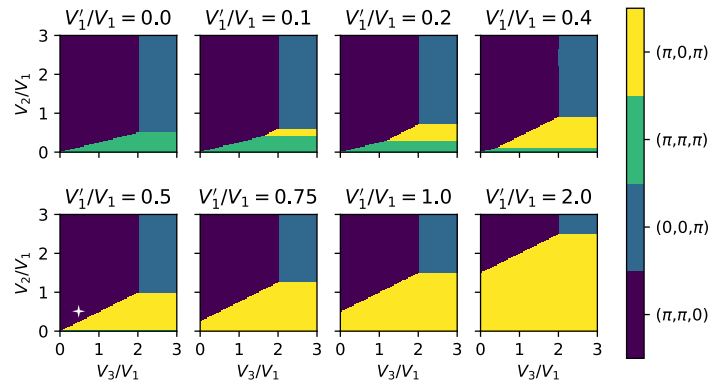


FIG. 10. (Color online) Phase diagram showing the lowest-energy mode (degenerate with symmetry-related modes) resulting from a model of electrostatic charges subject to the interaction of Eq. 9. Ordering wavevectors are expressed in x , y , and z components with $a_0 = c = 1$. The white star shows the relative parameter values used in the MF calculation.

to the following MF interaction term:

$$V_{\text{MF}} = \frac{1}{2} \sum_{(i,\alpha) \neq (j,\beta)} V_{ij}^{\alpha\beta} \left(\rho_i^\alpha n_j^\beta + n_i^\alpha \rho_j^\beta \right) \quad (\text{B1a})$$

$$= N \sum_{\mathbf{q}} \sum_{\alpha\beta} V_{\mathbf{q}}^{\alpha\beta} \rho_{\mathbf{q}}^{\alpha*} n_{\mathbf{q}}^\beta. \quad (\text{B1b})$$

Here, N is the number of unit cells in the crystal, $\rho_{\mathbf{q}}^\alpha = N^{-1} \sum_i e^{-i\mathbf{q} \cdot \mathbf{R}_i} \rho_i^\alpha$ (and likewise for $n_{\mathbf{q}}^\alpha$), and $V_{\mathbf{q}}^{\alpha\beta}$ is the Fourier transform of $V_{ij}^{\alpha\beta}$, which is invariant under simultaneous translation of i and j .

Choosing a closed set of commensurate wavevectors $\{\mathbf{Q}\}$ defines a *reduced Brillouin zone* (RBZ), which is mapped to the full Brillouin zone under addition of the wavevectors \mathbf{Q} . This property allows us to rewrite the integral of reciprocal-space-periodic functions as

$$\sum_{\mathbf{k}}^{\text{BZ}} f(\mathbf{k}) = \sum_{\mathbf{Q}} \sum_{\mathbf{k}}^{\text{RBZ}} f(\mathbf{k} + \mathbf{Q}), \quad (\text{B2})$$

where the domain of the momentum sums is indicated above the summation symbol. Hence, we diagonalized the Hamiltonian $H_{\text{MF}} = K + V_{\text{MF}}$ in the RBZ by writing it in the form

$$K = \sum_{\mathbf{k}}^{\text{RBZ}} \sum_{\alpha\beta} \sum_{\mathbf{Q}} c_{\mathbf{k}+\mathbf{Q}}^\alpha \dagger h_{\mathbf{k}+\mathbf{Q}}^{\alpha\beta} c_{\mathbf{k}+\mathbf{Q}}^\beta \quad (\text{B3})$$

$$V_{\text{MF}} = \sum_{\mathbf{k}}^{\text{RBZ}} \sum_{\alpha} \sum_{\mathbf{Q}\mathbf{Q}'} c_{\mathbf{k}+\mathbf{Q}}^\alpha \dagger \tilde{\rho}_{\mathbf{Q}-\mathbf{Q}'}^\alpha c_{\mathbf{k}+\mathbf{Q}}^\alpha, \quad (\text{B4})$$

where $\tilde{\rho}_{\mathbf{Q}}^{\alpha} = \sum_{\beta} V_{\mathbf{Q}}^{\alpha\beta} \rho_{\mathbf{Q}}^{\beta}$ and $h_{\mathbf{k}}^{\alpha\beta}$ is the Bloch Hamiltonian, in our case given in Eq. 7: $h_{\mathbf{k}} = d_{\mathbf{k}}^0 + \vec{d}_{\mathbf{k}} \cdot \vec{\tau}$. Starting from a series of randomized values for the MFs $\rho_{\mathbf{Q}}^{\alpha}$, we iterated until

the computed expectation values agree with the input MFs to within 10^{-6} . We compared the Helmholtz free energy F of the different ground states thusly obtained and selected the one with minimal F at every point in parameter space.

-
- ¹ Nicola A. Spaldin and Manfred Fiebig, “The renaissance of magnetoelectric multiferroics,” *Science* **309**, 391–392 (2005).
 - ² W. Eerenstein, N. D. Mathur, and J. F. Scott, “Multiferroic and magnetoelectric materials,” *Nature* **442**, 759–765 (2006).
 - ³ Ramaroorthy Ramesh and Nicola A. Spaldin, “Multiferroics: Progress and prospects in thin films,” *Nature materials* **6**, 21 (2007).
 - ⁴ Sang-Wook Cheong and Maxim Mostovoy, “Multiferroics: a magnetic twist for ferroelectricity,” *Nature Materials* **6**, 13 (2007).
 - ⁵ Nicola A. Spaldin, Sang-Wook Cheong, and Ramamoorthy Ramesh, “Multiferroics: Past, present, and future,” *Physics Today* **63**, 38–43 (2010).
 - ⁶ G. Lawes and G. Srinivasan, “Introduction to magnetoelectric coupling and multiferroic films,” *Journal of Physics D: Applied Physics* **44**, 243001 (2011).
 - ⁷ L. E. Fuentes-Cobas, J. A. Matutes-Aquino, M. E. Botello-Zubiate, A. González-Vázquez, M. E. Fuentes-Montero, and D. Chateigner, “Chapter 3 - advances in magnetoelectric materials and their application,” in *Handbook of Magnetic Materials*, Vol. 24, edited by K. H. J. Buschow (Elsevier, 2015) pp. 237–322.
 - ⁸ Zhaoqiang Chu, MohammadJavad PourhosseiniAsl, and Shuxiang Dong, “Review of multi-layered magnetoelectric composite materials and devices applications,” *Journal of Physics D: Applied Physics* **51**, 243001 (2018).
 - ⁹ M. Zahid Hasan and Charles L. Kane, “Colloquium: Topological insulators,” *Reviews of Modern Physics* **82**, 3045 (2010).
 - ¹⁰ Xiao-Liang Qi and Shou-Cheng Zhang, “Topological insulators and superconductors,” *Reviews of Modern Physics* **83**, 1057 (2011).
 - ¹¹ Adolfo G. Grushin and Fernando de Juan, “Finite-frequency magnetoelectric response of three-dimensional topological insulators,” *Physical Review B* **86**, 075126 (2012).
 - ¹² D. A. Pesin and A. H. MacDonald, “Topological magnetoelectric effect decay,” *Physical Review Letters* **111**, 016801 (2013).
 - ¹³ D. Schmeltzer and Avadh Saxena, “Magnetoelectric effect induced by electron–electron interaction in three dimensional topological insulators,” *Physics Letters A* **377**, 1631–1636 (2013).
 - ¹⁴ A. G. Mal’Shukov, Hans Skarsvåg, and Arne Brataas, “Nonlinear magneto-optical and magnetoelectric phenomena in topological insulator heterostructures,” *Physical Review B* **88**, 245122 (2013).
 - ¹⁵ Dashdeleg Baasanjav, O. A. Tretiakov, and Kentaro Nomura, “Magnetoelectric effect in topological insulator films beyond the linear response regime,” *Physical Review B* **90**, 045149 (2014).
 - ¹⁶ Takahiro Morimoto, Akira Furusaki, and Naoto Nagaosa, “Topological magnetoelectric effects in thin films of topological insulators,” *Physical Review B* **92**, 085113 (2015).
 - ¹⁷ Di Xiao, Jue Jiang, Jae-Ho Shin, Wenbo Wang, Fei Wang, Yi-Fan Zhao, Chaoxing Liu, Weida Wu, Moses H. W. Chan, Nitin Samarth, and Cui-Zu Chang, “Realization of the axion insulator state in quantum anomalous Hall sandwich heterostructures,” *Physical Review Letters* **120**, 056801 (2018).
 - ¹⁸ Yoshinori Tokura, Kenji Yasuda, and Atsushi Tsukazaki, “Magnetic topological insulators,” *Nature Reviews Physics* **1**, 126–143 (2019).
 - ¹⁹ L. S. Levitov, Yu V. Nazarov, and G. M. Eliashberg, “Magnetoelectric effects in conductors with mirror isomer symmetry,” *Sov. Phys. JETP* **61**, 133–137 (1985).
 - ²⁰ C. Şahin, J. Rou, J. Ma, and D. A. Pesin, “Pancharatnam-Berry phase and kinetic magnetoelectric effect in trigonal tellurium,” *Physical Review B* **97**, 205206 (2018).
 - ²¹ Jairo Sinova, Sergio O. Valenzuela, J. Wunderlich, C. H. Back, and T. Jungwirth, “Spin Hall effects,” *Reviews of Modern Physics* **87**, 1213 (2015).
 - ²² Aurelien Manchon, Hyun Cheol Koo, Junsaku Nitta, S. M. Frolov, and R. A. Duine, “New perspectives for Rashba spin-orbit coupling,” *Nature Materials* **14**, 871 (2015).
 - ²³ Sergey D. Ganichev, Maxim Trushin, and John Schliemann, “Spin polarisation by current,” in *Handbook of Spin Transport and Magnetism*, edited by Evgeny Y. Tsymlal and Igor Zutic (Chapman and Hall/CRC, 2016) 2nd ed., pp. 504–513.
 - ²⁴ Y. K. Kato, R. C. Myers, A. C. Gossard, and D. D. Awschalom, “Current-induced spin polarization in strained semiconductors,” *Physical Review Letters* **93**, 176601 (2004).
 - ²⁵ A. Yu Silov, P. A. Blajnov, J. H. Wolter, R. Hey, K. H. Ploog, and N. S. Averkiev, “Current-induced spin polarization at a single heterojunction,” *Applied Physics Letters* **85**, 5929–5931 (2004).
 - ²⁶ Y. K. Kato, R. C. Myers, A. C. Gossard, and D. D. Awschalom, “Electrical initialization and manipulation of electron spins in an L-shaped strained *n*-InGaAs channel,” *Applied Physics Letters* **87**, 022503 (2005).
 - ²⁷ Vanessa Sih, R. C. Myers, Y. K. Kato, W. H. Lau, A. C. Gossard, and D. D. Awschalom, “Spatial imaging of the spin Hall effect and current-induced polarization in two-dimensional electron gases,” *Nature Physics* **1**, 31 (2005).
 - ²⁸ N. P. Stern, S. Ghosh, G. Xiang, M. Zhu, N. Samarth, and D. D. Awschalom, “Current-induced polarization and the spin Hall effect at room temperature,” *Physical Review Letters* **97**, 126603 (2006).
 - ²⁹ C. L. Yang, H. T. He, Lu Ding, L. J. Cui, Y. P. Zeng, J. N. Wang, and W. K. Ge, “Spectral dependence of spin photocurrent and current-induced spin polarization in an InGaAs/InAlAs two-dimensional electron gas,” *Phys. Rev. Lett.* **96**, 186605 (2006).
 - ³⁰ H. J. Zhang, S. Yamamoto, Y. Fukaya, M. Maekawa, H. Li, A. Kawasuso, T. Seki, E. Saitoh, and K. Takahashi, “Current-induced spin polarization on metal surfaces probed by spin-polarized positron beam,” *Scientific Reports* **4**, 4844 (2014).
 - ³¹ V. A. Shalygin, A. N. Sofronov, L. E. Vorob’ev, and I. I. Farbshtein, “Current-induced spin polarization of holes in tellurium,” *Physics of the Solid State* **54**, 2362–2373 (2012).
 - ³² Tetsuya Furukawa, Yuri Shimokawa, Kaya Kobayashi, and Tet-

- suaki Itou, “Observation of current-induced bulk magnetization in elemental tellurium,” *Nature Communications* **8**, 954 (2017).
- ³³ Taiki Yoda, Takehito Yokoyama, and Shuichi Murakami, “Current-induced orbital and spin magnetizations in crystals with helical structure,” *Scientific Reports* **5**, 12024 (2015).
- ³⁴ Shudan Zhong, Joel E. Moore, and Ivo Souza, “Gyrotropic magnetic effect and the magnetic moment on the Fermi surface,” *Physical Review Letters* **116**, 077201 (2016).
- ³⁵ J. Rou, C. Şahin, J. Ma, and D. A. Pesin, “Kinetic orbital moments and nonlocal transport in disordered metals with nontrivial band geometry,” *Physical Review B* **96**, 035120 (2017).
- ³⁶ Taiki Yoda, Takehito Yokoyama, and Shuichi Murakami, “Orbital Edelstein effect as a condensed-matter analog of solenoids,” *Nano Letters* **18**, 916–920 (2018).
- ³⁷ Stepan S. Tsirkin, Pablo Aguado Puente, and Ivo Souza, “Gyrotropic effects in trigonal tellurium studied from first principles,” *Physical Review B* **97**, 035158 (2018).
- ³⁸ Felix Flicker, Fernando de Juan, Barry Bradlyn, Takahiro Morimoto, Maia G. Vergniory, and Adolfo G. Grushin, “Chiral optical response of multifold fermions,” *Physical Review B* **98**, 155145 (2018).
- ³⁹ Chengwang Niu, Jan-Philipp Hanke, Patrick M. Buhl, Hongbin Zhang, Lukasz Plucinski, Daniel Wortmann, Stefan Blügel, Gustav Bihlmayer, and Yuriy Mokrousov, “Mixed topological semimetals and orbital magnetism in two-dimensional spin-orbit ferromagnets,” *arXiv e-prints*, arXiv:1805.02549 (2018), arXiv:1805.02549 [cond-mat.mes-hall].
- ⁴⁰ Li-kun Shi and Justin C. W. Song, “Symmetry, spin-texture, and tunable quantum geometry in a WTe_2 monolayer,” *Physical Review B* **99**, 035403 (2019).
- ⁴¹ Ana Silva, Jans Henke, and Jasper van Wezel, “Elemental chalcogens as a minimal model for combined charge and orbital order,” *Physical Review B* **97**, 045151 (2018).
- ⁴² Martin Gradhand and Jasper van Wezel, “Optical gyrotropy and the nonlocal Hall effect in chiral charge-ordered $TiSe_2$,” *Physical Review B* **92**, 041111 (2015).
- ⁴³ J. Orenstein and Joel E. Moore, “Berry phase mechanism for optical gyrotropy in stripe-ordered cuprates,” *Physical Review B* **87**, 165110 (2013).
- ⁴⁴ Raffaele Resta, “Electrical polarization and orbital magnetization: the modern theories,” *Journal of Physics: Condensed Matter* **22**, 123201 (2010).
- ⁴⁵ T. Thonhauser, “Theory of orbital magnetization in solids,” *International Journal of Modern Physics B* **25**, 1429–1458 (2011).
- ⁴⁶ David Vanderbilt, *Berry Phases in Electronic Structure Theory: Electric Polarization, Orbital Magnetization and Topological Insulators* (Cambridge University Press, 2018).
- ⁴⁷ Raffaele Resta, “Electrical polarization and orbital magnetization: The position operator tamed,” *Handbook of Materials Modeling: Methods: Theory and Modeling*, 1–31 (2018).
- ⁴⁸ Di Xiao, Ming-Che Chang, and Qian Niu, “Berry phase effects on electronic properties,” *Reviews of Modern Physics* **82**, 1959 (2010).
- ⁴⁹ Neil W. Ashcroft and N. David Mermin, *Solid State Physics* (Holt, Rinehart and Winston, 1976).
- ⁵⁰ John Frederick Nye, *Physical Properties of Crystals: Their Representation by Tensors and Matrices* (Oxford University Press, 1957).
- ⁵¹ L. D. Landau and E. M. Lifshitz, *Electrodynamics of Continuous Media*, Course of Theoretical Physics, Vol. 8 (Pergamon Press, 1960).
- ⁵² Takayuki Ishitobi and Kazumasa Hattori, “Magneto-electric Effects and Charge-imbalanced Solenoids: Antiferro Quadrupole Orders in a Diamond Structure,” *arXiv e-prints*, arXiv:1903.01103 (2019), arXiv:1903.01103 [cond-mat.str-el].